Motion estimation of subcellular structures from fluorescence microscopy images

A. Vallmitjana[1], A. Civera-Tregón[2,3], J. Hoenicka[2], F. Palau[3,4] and R. Benítez[1]

Abstract— We present an automatic image processing framework to study moving intracellular structures from live cell fluorescence microscopy. The system includes the identification of static and dynamic structures from time-lapse images using data clustering as well as the identification of the trajectory of moving objects with a probabilistic tracking algorithm. The method has been successfully applied to study mitochondrial movement in neurons. The approach provides excellent performance under different experimental conditions and is robust to common sources of noise including experimental, molecular and biological fluctuations.

I. INTRODUCTION

Live cell imaging from time-lapse fluorescence microscopy is a widely available experimental technique to study of cell function and disease [1]. Recent advances in super-resolution microscopy allow the localization of static subcellular structures with a resolution under the diffraction limit [2]. However, cell function is not fully determined by static features such as the localization, shape or spatial distribution of subcellular structures but also by their intrinsic dynamical behaviour. In particular, there is an emerging interest in further understanding dynamical scenarios associated to phenomena such as vesicle trafficking pathways [3], cell signaling [4] or intracellular calcium dynamics [5].

To this extent, current biological studies require advanced characterization of dynamic subcellular structures from live cell fluorescence imaging [6]. The aim of our study is to provide a robust framework for the quantitative motion estimation of subcellular structures from fluorescence microscopy images. Previous studies have mostly focused in the use of optical flow methods in combination of random markov field models [7], [8], [9], [10]. However, such algorithms typically require a high frame rate image acquisition system in order to properly estimate the velocities of the moving objects. In this study we focus in the rather frequent case in which experimental set-up has a low sampling sample rate with respect to the motion of the structures of interest.

As a proof of concept, we apply the method to the motion tracking of mitochondria. Mitochondrial trafficking in neurons constitutes a clear example of subcellular structures whose motion determines functional properties of the system [11]. However, characterization of mitochondrial dynamics requires manual tracking by an expert and is time-consuming and prone to human errors. Previous automatic methods develop a probabilistic estimation of mitochondrial motion [10]. Mitochondria have a critical role in the pathogenesis of neurodegeneration [12]. Preliminary results indicate abnormal movement of mitochondria along the cytoskeleton in mouse embryonic motor neurons having no GDAP1 expression [13].

II. EXPERIMENTAL SETUP

A. *Experimental data*

A total of 88 experiments were recorded at a sampling period of $5.26s$ an image size of 1024×128 pixels, a physical pixel size of $0.12 \mu m$ and 16-bit depth. 32 experiments were recorded during a period of 5 minutes (57 frames) and 56 experiments during 131 seconds (25 frames). Figure 1 shows an example image of one of the experiments (Fig.1, upper panel), where a region of interest has been selected in which a mitochondria is moving from right to left (lower panels, time sequence evolves from left to right).

B. *Image acquisition*

In-vivo mitochondrial movement in neurons was experimentally studied using microfluidic chambers. The microfluidic device is composed of two open culture chambers connected by a parallel array of microchannels. The system allows fluidic separation of axons from the soma and permits observing mitochondrial movement along oriented axons. Axonal microchannels were labeled with the mitochondria-specific dye (Mitotracker Green) and recorded in a climate controlled chamber (In Vivo Scientific) at $37°C$ and 5% CO_2 using conventional confocal microscopy (SP2, Leica). Fluorescent marker was stimulated using a 488nm argon laser and the optical setup included a $\times 63$ oil immersion lens with $\times 2$ zoom and a pinhole of 1 AU.

C. *Embryonic motor neuron primary culture*

Embryonic motor neuron (MN) cultures MN cultures were prepared from 13.5 embryonic day (E13.5) mouse spinal cord. Briefly, mouse embryo spinal cords were dissected and the dorsal half removed. Ventral spinal cords were dissociated mechanically after trypsin treatment (0.025% trypsin in HBSS), and collected afterwards under a 4% bovine serum albumin cushion. The largest cells were isolated by centrifugation (10 min at 520 g) using iodixanol density gradient purification. The collected cells were finally suspended

[1]Biomedical Engineering Research Center, Universitat Politècnica de Catalunya and Institut de Recerca Sant Joan de Déu, Barcelona, Spain raul.benitez@upc.edu

[2]Neurogenetics and Molecular Medicine, Institut de Recerca Sant Joan de Déu, Barcelona, Spain

[3]CIBERER, Barcelona, Spain

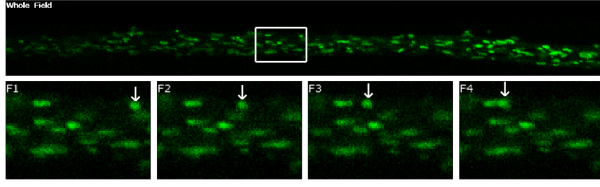[4]Division of Pediatrics, Universitat de Barcelona, Barcelona, Spain

Fig. 1. Example of mitochondrial movement. Lower panels labeled as F1-F4 are four consecutive frames showing the time evolution of the selected region of interest from the whole field image. Arrows indicate the position of the structure in each frame.

in a tube containing MN complete medium: Neurobasal (Life technologies) supplemented with B27 (Life technologies), 2% horse serum, 1x glutamax (Life technologies), and a cocktail of recombinant neurotrofins: 1ng/mL BDNF; 10ng/mL GDNF, 10ng/mL CNTF, and 10ng/mL HGF (Pre-Protech). $10\mu M$ AraC (Sigma-Aldrich) was added to the culture medium to limit the growth of non-neuronal cells. MNs (3×10^5 cells) were added to the proximal chamber of prepared microfluidic devices and grown in a 5% CO_2 incubator at 37°C.

D. Preparation of Microfluidic chamber

Microfluidic devices with 450nm microgroves (Xona Microfluidic, Catalog SND450) were cleaned of surface particles using adhesive tape and sterilized in 70% ethanol for 2-3 hours. Devices were dried completely under sterile conditions, attached to treated Poli-L-ornithine sterile $22mm^2$ coverslips (Thermoscientific) using gentle pressure from blunt sterile forceps and placed in 6 well culture. Each device was designated a proximal and distal side. Chamber were filled with neuron medium and equilibrated for 2 hours. The medium was removed and Laminin was added and incubated overninght at 37°C. Laminin was removed prior to addition of neurons.

III. METHODOLOGY

The image processing pipeline for characterising biological structure trafficking is described in detail in the following subsections.

A. Preprocessing

For each experiment the complete image sequence is initially loaded in the form of a spatio-temporal volume and the subsequent processing operations are performed in 3D. First, convolution by a Gaussian filter in the spatial dimensions is applied with $\sigma = 0.2\mu m$ (a filter of $3\times3\times1$ voxels) in order to reduce noise in the images and obtain smooth surfaces for object segmentation. The size of the filter is a parameter that should be tuned according to image noise conditions, image resolution and the size of the target object of interest. Figure 2a depicts the result of the filtering in a sample region of interest.

B. Coarse segmentation

An initial coarse segmentation method is applied to each frame. More specifically, we use a custom watershed technique with a stopping rule for the size and intensity of the

detected regions. Taking the image as a topological surface, the dark areas being the highest points and the bright objects being deeper regions, the method can be seen as if we were to flood the whole surface and then gradually reduce the water level. Any isolated *puddle* that is left is considered a candidate if it has a minimum size of $1\mu m^2$. These candidate regions are further subdivided by lowering even more the water level if the subregions have a minimum depth of at least 0.2 (normalized intensity). These two constraints were chosen in order to guarantee the physiological relevance of the segmented structures, and again, these parameters were selected in order to detect mitochondria in the images but should be modified to the particular structure under study.

C. Region properties

After segmentation, we obtain the centers of mass for each of the resulting regions (Fig.2b). The dimensions of each region are obtained from the intensity profiles along the two orthogonal directions X and Y intersecting at each center of mass. In these profiles, the diameter in each direction is defined as the full width at a third of the maximum (see Fig. 3). Halving the two measured diameters we obtain two radii that are then taken as the semi-axes of an ellipse which allows to estimate object area as πab with a and b being the two measured radii. Figure 2c is a representation of the equivalent ellipses for each detected object using the two radii.
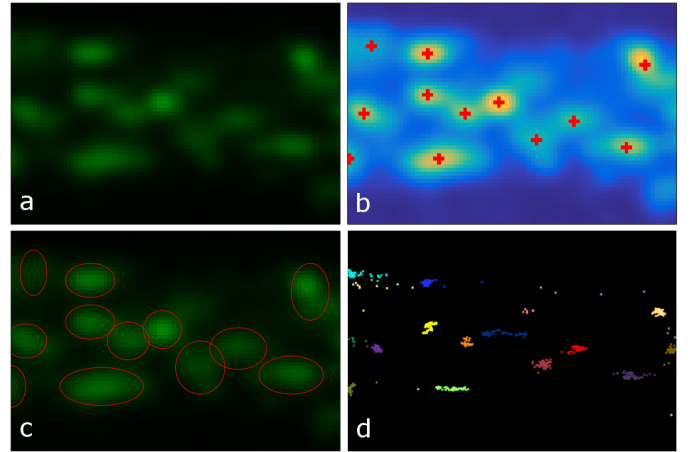

Fig. 2. Stages of the image processing pipeline using the region of interest of Fig. 1. The top-left panel (a) shows the sample crop of a single frame after pre-processing for noise removal. Top-right panel (b) pictures the same image in false colour with the centroid of detected objects after the watershed transform. In bottom-left panel (c), ellipses are drawn with the equivalent diameters after dimensions are estimated (see Fig. 3). The bottom-right panel (d) shows an X-Y projection of the centroids of segmented objects in all frames after clustering step is applied, i.e. the film is flattened in the temporal direction (colours are randomly selected to show different clusters). More clusters can be observed than the number of detected cells in panel 2b because the detected cells are shown from a single frame, whereas the clusters in 2d include detection in all frames. For this reason moving objects leave a trail of dots, seen in the top region, and in panel 2b the moving object appears detected in the top-right-most region. This trail will be assigned to a moving cluster because it does not contain enough elements (see section III-D). Also in the right-most region an object that in panel 2b is out of the cropped region appears.
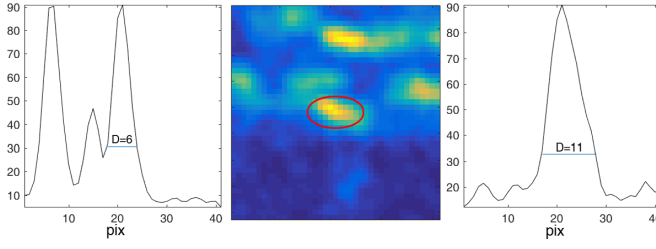
Fig. 3. Area estimation procedure. Transversal intensity profiles along the orthogonal directions (vertical direction in left panel and horizontal direction in right panel) of the region marked in the central panel. Diameter in each direction is set as the full width at a third of the maximum.
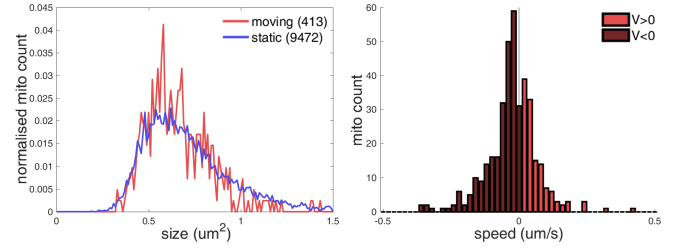

Fig. 4. Characterization of moving and static mitochondria. Size distribution of both moving and static (left panel). Velocity distribution of the moving mitochondria (right panel).

D. Moving vs. static structures: Spatial clustering of the centroid dynamics

In order to identify which structures are static or dynamic we perform a X-Y projection of the centroids of each region in each time frame, i.e. the X-Y coordinates of the detected centroids in all frames are represented in a single image. In this projection, static structures throughout the sequence appear as compact clusters whereas moving objects appear as isolated points. A hierarchical clustering is applied to this set of coordinates in order to identify static structures, by using a euclidean distance cutoff of $1.2\mu m$ in the vertical direction and $2.4\mu m$ in the horizontal direction. This asymmetry was used because in this particular case objects would tend to slightly drift in the horizontal direction and moreover they appeared elongated in that same direction. The clusters that contain a minimum number of elements correspond to static objects, whereas those that do not correspond to moving. This thresholding number depends on the frame rate since each element corresponds to a detection in one frame, and for this experiment it was set to the number of frames equivalent to 1 minute. The clustering step can be observed in the scatter plot represented in the Figure 2d where each centroid of a detected object is plotted in a different colour for each cluster.

E. Characterization of mitochondrial movement

The resulting clusters from the previous step are used to identify the static objects from the set of coordinates of detected objects. After removing the centroids belonging to the static structures, the remaining isolated X-Y-T centroid coordinates are assumed to correspond to the movement of a mitochondria. A probabilistic tracking approach is then used in order to cluster these isolated centroids into separate trajectories [14]. Association of objects from one frame to the next is performed using a Markov model in order to model the changes between consecutive frames in the position, velocity, area and intensity of the detected structures.

More specifically, given a pair of consecutive frames k and $k+1$, we model the probability of object labelled i in frame k corresponds to object labelled j in frame $k+1$. We express this probability in terms of the weighted normalized discrepancy of the features of the two objects in the two frames:

$$P_{ij}^k = 1 - \sum_{l=1}^{N_f} \omega_l \, \hat{d}_l$$

where N_f stands for the number of extracted features, ω_l is the weight assigned to feature f_l and $\hat{d}_l$ is the normalized feature discrepancy $\hat{d}_l = d_l/D_l$ with D_l being the normalization constant that depends on the particular feature and the discrepancy defined as the difference of the feature measured in the two consecutive frames $d_l = f_l(i,k) - f_l(j,k+1)$.

The particular features used in this case where position norm, velocity norm, area and mean intensity. The four weights were set equal to ω_l=0.25 and the normalizing values were established by the image dimensions: its diagonal for the position and velocity and the total number of pixels for the area. The intensity was normalized to unity. A minimum probability threshold is required to allow for occlusions and objects that enter/exit the field of view through the image limits or appear/disappear due to movement oblique to the focal plane. In this case the threshold was fixed at 0.8 but this value is highly dependant on the normalization values used in the tracking method. Figure 6 shows the results of the tracking method where objects that have not survived the clustering of static objects are assigned to separate trajectories depicted in red.
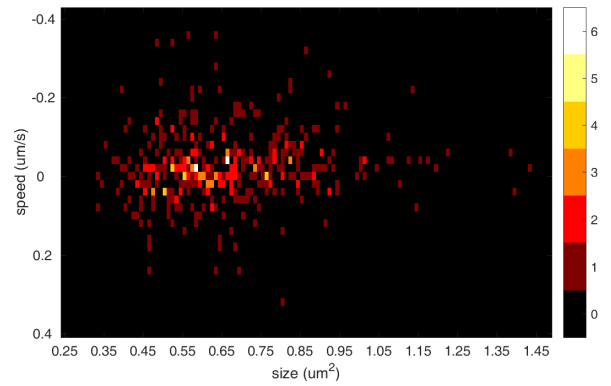

Fig. 5. Two dimensional histogram for the moving mitochondria depicting area versus speed representation.
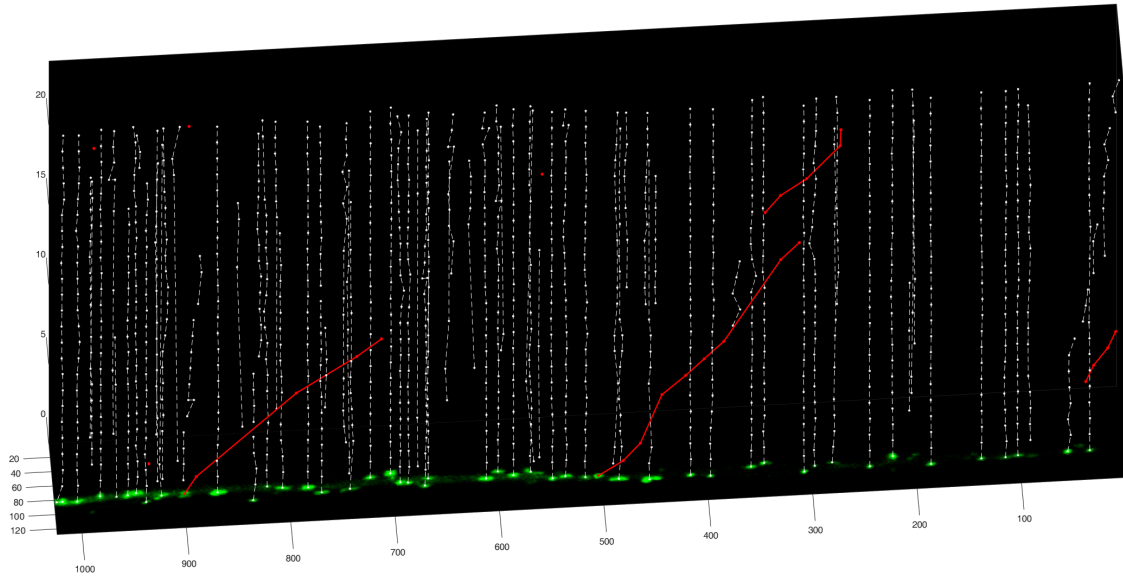
Fig. 6. After clustering static objects and tracking of moving objects, a 3D representation of the detected centroids in the image sequence clearly shows movement (X and Y axes are image spatial dimensions in pixels and the vertical axis is time in frames). Moving mitochondria are depicted as connected red lines and static mitochondria as connected white lines.

IV. RESULTS

The described technique is straightforward, computationally efficient and fast when compared to more complex methods. It can be used to robustly segment and characterise static objects and to track moving objects while measuring their speed.

In the particular case study the method size estimation for all detected objects was a mean of $0.72\mu m^2$ and a standard deviation of $0.26\mu m^2$ (9885 objects). As can be seen in Fig. 4 (left panel), a slight deviation is observed between moving and static mitochondria at the greater sizes, resulting in a statistically significant difference between the medians of the two distributions ($p < 0.01$, Wilcoxon ranksum test).

Regarding moving objects, it is evident that there is an asymmetry in the movement (see figure 4, right panel) since there is a considerably larger number of mitochondria travelling towards the left than in the opposite direction (63%), mean speed of $-0.023um/s$ (confidence interval at 95% confidence level is $[-0.0316 \ -0.0144]um/s$). Figure 5 represents a combined 2D histogram of speed versus area for all moving mitochondria analyzed in the study.

V. CONCLUSIONS

We have developed and validated a suitable approach for the detection and tracking of subcellular structures. Application to mitochondrial trafficking in neurons indicates that the approach is both robust and accurate, thus suitable for most practical applications.

Further development is required to capture specific dynamical features of mitochondrial motion such as objects that belong to both moving and static in different time periods during the experiment. In our case, this limitation results in an over estimation of the total number of objects.

REFERENCES

[1] D. J. Stephens and V. J. Allan, "Light microscopy techniques for live cell imaging," *Science*, vol. 300, no. 5616, pp. 82–86, 2003.

[2] A. G. Godin, B. Lounis, and L. Cognet, "Super-resolution microscopy approaches for live cell imaging," *Biophysical journal*, vol. 107, no. 8, pp. 1777–1784, 2014.

[3] A. A. Tokarev, A. Alfonso, and N. Segev, "Overview of intracellular compartments and trafficking pathways," in *Trafficking Inside Cells*. Springer, 2009, pp. 3–14.

[4] Z. E. Perlman, M. D. Slack, Y. Feng, T. J. Mitchison, L. F. Wu, and S. J. Altschuler, "Multidimensional drug profiling by automated microscopy," *Science*, vol. 306, no. 5699, pp. 1194–1198, 2004.

[5] J. P. Keener and J. Sneyd, *Mathematical physiology*. Springer, 2009, vol. 1.

[6] A. M. Derfus, W. C. Chan, and S. N. Bhatia, "Intracellular delivery of quantum dots for live cell labeling and organelle tracking," *Advanced Materials*, vol. 16, no. 12, pp. 961–966, 2004.

[7] E. Lihavainen, J. Mäkelä, J. N. Spelbrink, and A. S. Ribeiro, "Mytoe: automatic analysis of mitochondrial dynamics," *Bioinformatics*, vol. 28, no. 7, pp. 1050–1051, 2012.

[8] J. Delpiano, J. Jara, J. Scheer, O. A. Ramírez, J. Ruiz-del Solar, and S. Härtel, "Performance of optical flow techniques for motion analysis of fluorescent point signals in confocal microscopy," *Machine Vision and Applications*, vol. 23, no. 4, pp. 675–689, 2012.

[9] F. Amat, E. W. Myers, and P. J. Keller, "Fast and robust optical flow for time-lapse microscopy using super-voxels," *Bioinformatics*, vol. 29, no. 3, pp. 373–380, 2013.

[10] J. H. Broeke, H. Ge, I. M. Dijkstra, A. T. Cemgil, J. A. Riedl, L. N. Cornelisse, R. F. Toonen, M. Verhage, and W. J. Fitzgerald, "Automated quantification of cellular traffic in living cells," *Journal of neuroscience methods*, vol. 178, no. 2, pp. 378–384, 2009.

[11] T. L. Schwarz, "Mitochondrial trafficking in neurons," *Cold Spring Harbor Perspectives in Biology*, vol. 5, no. 6, p. a011304, 2013.

[12] E. A. Schon and S. Przedborski, "Mitochondria: the next (neurode) generation," *Neuron*, vol. 70, no. 6, pp. 1033–1053, 2011.

[13] M. Barneo-Muñoz, P. Juárez, A. Civera-Tregón, L. Yndriago, D. Pla-Martín, J. Zenker, C. Cuevas-Martín, A. Estela, M. Sánchez-Aragó, J. Forteza-Vila *et al.*, "Lack of gdap1 induces neuronal calcium and mitochondrial defects in a knockout mouse model of charcot-marie-tooth neuropathy," *PLoS Genet*, vol. 11, no. 4, p. e1005115, 2015.

[14] R. Benítez, A. Vallmitjana, L. Hove-Madsen, and P. P. Jones, "Detection and classification of spontaneous calcium release events in cardiac myocytes," *Biophysical Journal Sup. 1*, vol. 102, no. 3, p. 309, 2012.